2024 IEEE/RSJ International Conference on Intelligent Robots and Systems (IROS)
October 14-18, 2024. Abu Dhabi, UAE

An Ejecting System for Autonomous Takeoff of Flapping-Wing Robots

Xu Jiang, *Student Member, IEEE*, Jun Zhang, *Senior Member, IEEE*, and Aiguo Song, *Senior Member, IEEE*

***Abstract*—Autonomous takeoff of flapping-wing robots (FWRs) is crucial for accelerating response speed and reducing costs in executing tasks. Jumping-aided takeoff is an effective method adopted by birds. However, the limited power density of motors poses challenges in achieving this type of takeoff for FWRs. In this study, we introduce a ground-based FWR ejecting system that utilizes a symmetric slider-crank mechanism (S-SCM) to store energy in spring. This stored energy is then converted into the takeoff speed of the FWR. The dynamic model of each working stage is established, and the design parameters are optimized according to simulation results. The prototype of the FWR ejecting system is fabricated for experimental validations. The results indicate that the system can provide a takeoff speed of 4 m/s for the 270 g FWR. Notably, the system is deployable on rough terrains and only adds a 3.2 g payload to the robot. Our work advances the autonomous takeoff of FWRs, promoting the application of such robots.**

I. Introduction

Flapping-wing robots (FWRs) offer distinct benefits, such as reduced noise emissions and improved safety, making them suitable for search and reconnaissance. In recent years, FWR technology has rapidly evolved towards high maneuverability, heavy payload capacity, and autonomous flight capabilities. For instance, Karásek et al. achieved three-axis attitude control of flapping wings in mid-air with a unique mechanism mimicking the rapid maneuvers of fruit flies [1]. Ozaki et al. developed a 2.1-g micro-aerial vehicle driven by piezoelectric actuators, being the first untethered FWR at this scale [2]. The USTBird has two servos that independently control the wings, enabling better emulation of bio-inspired motions such as diving and gliding [3]. The E-flap robot can carry up to 0.5 kg, highlighting its load capacity [4]. The Bat Bot features bionic passive joints and elastic fiber membranes [5]. Furthermore, new methods for developing FWRs cover twisted and folded wings [6], efficient aerodynamic modeling methods [7], and event-based visual perception [8].

Existing FWRs can be mainly classified into insect-like robots [1], [2]and bird-like robots [3], [4]. The insect-like robots possess wings flapping around the vertical axes, directly providing upward lift force when taking off, thus enabling the robot to hover in the air. In contrast, the bird-like robots flap their wings around the 'spine.' The generated force is decomposed into the lift force and thrust depending on the attack angle. Like the E-Flap, some bird-like wings are designed as curved surfaces to improve the aerodynamic characteristics [4]. Nonetheless, the bird-like FWRs are challenged because the wings cannot provide sufficient lift force during takeoff. Manual throwing is the basic method to generate the takeoff velocity [9], which costs workforce and training efforts. This greatly restricts the application of FWRs.

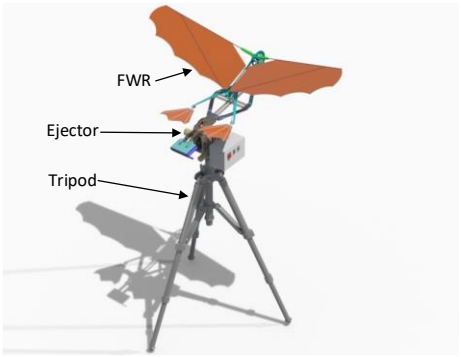

Fig. 1. Conceptual model of the flapping-wing robot (FWR) ejector.

Efforts devoted to the autonomous takeoff of bird-like FWRs have made prominent achievements. Ma et al. classified the takeoff methods of FWR into jumping, running, gliding, and vertical takeoff [10]. They then provided a solution for vertical takeoff by adding four rotors to the FWR. Vertical takeoff is suitable for insect-like FWRs as these robots are lightweight (less than 50 g) and can be lifted by their wings. Afakh et al. first realized the self-takeoff of a bird-like FWR at the initial pitch angle of 60° [11]. The pitching moment generated by wing-flapping was neutralized through structural optimizations. However, their method for the 96-g robot may not suit heavier robots.

Although the gliding takeoff method has not been realized yet, Zufferey et al. have realized autonomous branch-perching of an FWR [4], laying a prerequisite for this takeoff approach. The USTBird adopted the running takeoff method [3], with a four-wheel carrier providing the initial velocity. Our lab also gave a running takeoff solution using a two-wheel structure attached to the robot [12]. The wheeled-running method suits flat, paved surfaces but not natural terrains. The foot-running takeoff offers a potential solution for unstructured terrain. However, the limited power density of the motor poses

This work was supported in part by the National Natural Science Foundation of China under Grants 61873066 and 62173090, and the Fundamental Research Funds for the Central Universities 2242024K40039.

The authors are with State Key Laboratory of Digital Medical Engineering, Jiangsu Key Lab of Robot Sensor and Control, School of Instrument Science and Engineering, Southeast University, Nanjing 210096, China (e-mail: xjiang@seu.edu.cn, j.zhang@seu.edu.cn., a.g.song@seu.edu.cn).

difficulty in reducing weight. No significant breakthroughs have been achieved.

To take off with a jump, the initial velocity is provided by a jumping mechanism. Our lab explored the jumping takeoff method with a multiple parallelogram mechanism mounted on the robot [13]. The mechanism uses the motor power source of the wings, reducing the robot's weight. Zhao et al. realized takeoff with a compressed air launcher [14]. This approach is efficient and portable, but the folding mechanism may affect the robot's flying performance.

As shown in Fig. 1, we develop an FWR ejector as the initial effort toward an autonomous launch and recovery system for bird-like FWRs. Tensile springs are used as the energy storage medium. The ejector is deployed on a tripod and can be positioned in rough terrains. The system only requires the addition of a 3.2-g component to the FWR, freeing up precious load space. The contributions include:

1) Establishing models for the charging and ejecting stages and conducting simulations. The symmetric slider-crank mechanism (S-SCM) reduces the motor's load. The structure of the mechanism is optimized to improve efficiency.

2) Experimenting with the charging, ejecting, and takeoff operations. The recharging process takes 18 seconds. The ejector generates a velocity of 4 m/s for the 270-g robot to take off. The ejecting takeoff method has better efficiency and success rate than the manual throwing method.

II. Modeling and Optimization

Bionic jumping robots store energy in elastic components. Inspired by [15], we use an S-SCM to charge and release spring energy.

A. Modeling of the Ejecting Mechanism

As shown in Fig. 2, the S-SCM comprises the root link, slider, guide rail, side links, spring, and rope. The root link is fixed at the origin of frame xOy. The guide rail restricts the slider to move along the Y-axis. At each side of the rail, two side links connect the root link to the slider, forming a slider-crank mechanism. Besides, the tensile spring is installed between the joints connecting the side links. The FWR is installed on the slider through a slot structure. Therefore, the system has one degree of freedom. The system's state is described by the angle θ between the X-axis and the bottomed side link. The ejector's pitch angle α is the difference between the xOy plane and the horizontal plane.

A takeoff operation consists of the charging, ejecting, and takeoff stages. In the charging stage, a rope pulls the slider toward the negative Y-axis. During the ejecting stage, the rope is released, triggering the spring to propel the slider and FWR forward. When the spring returns to its original length, the FWR detaches from the slider. In the takeoff stage, the FWR flaps its wings and ascends into the air.

In Fig. 2, a is the length of each side link, and b is the length of the root link and slider. m_1, m_2, and m_3 are the masses of the bottomed link, topped link, and slider, respectively. The robot

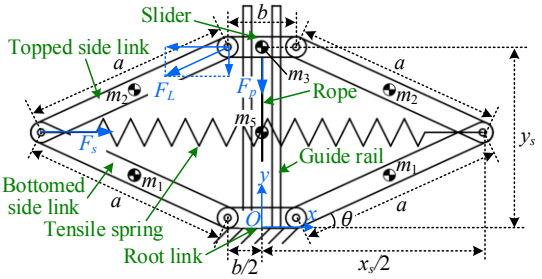

Fig. 2. Model of the symmetric slider-crank mechanism (S-SCM).

has a mass of m_4, and the spring weighs m_5. The rotational inertia of the rope is J_w. The spring has an original length of x_0 and a tensile elasticity of k. y_s is the Y-axis coordinate of the slider, and x_s is the length of the spring.

In the charging stage, the system is in a static balance. As shown in Fig. 2, F_L is the force endured by the side link. Decomposing force F_L, we find the X-axis component is balanced by the force of the spring (F_s), and the Y-axis component is balanced by the rope's pulling force (F_x). According to the law of force balance and the Pythagorean theorem, two equations are formulated as

$$\begin{cases} F_x / F_p = (x_s - b)/y_s \\ (y_s/2)^2 + ((x_s - b)/2)^2 = a^2 \end{cases} \tag{1}$$

Solving (1) derives the expression of the rope's pulling force:

$$F_p = y_s k(1 + (b - x_0)/\sqrt{4a^2 - y_s^2}) \tag{2}$$

The maximum pulling force in the charging stage is

$$F_{pm} = \max(F_p) = 2ka\left(1 - \left(\frac{x_0 - b}{2a}\right)^{2/3}\right)^{3/2} \tag{3}$$

The ejecting process is modeled by the Newton-Lagrange equation:

$$\begin{cases} L = E_k - E_p \\ \dfrac{d}{dt}\left(\dfrac{\partial L}{\partial \dot{\theta}}\right) - \dfrac{\partial L}{\partial \theta} = 0 \end{cases} \tag{4}$$

where L is the Newton-Lagrange function, E_k is the kinetic energy considering the masses of the slider, robot, side links, spring, and rope winch. E_p is the potential energy, which includes the moving components' gravitational energy and the spring's elastic energy. The dynamic model is expressed by an ordinary differential equation:

$$M(\theta)\ddot{\theta} + C(\theta, \dot{\theta}) + G(\theta) = 0 \tag{5}$$

where M, C, and G are the inertia, centripetal, and gravity coefficients, respectively.

B. Simulation of the Charging and Ejecting Stages

The charging stage was simulated with a = 154 mm, b = 60 mm, k = 550 N/m, x_0 = 151 mm, α = 9 °, m_1 = 46 g, m_2 = 66 g, m_3 = 50 g, m_4 = 450 g, m_5 = 99 g, $J_w = 1.28\times10^{-4}$ kg·m^2. Fig. 3(a) shows the variation of the rope-pulling force. The slider is initially located at y_s = 0.3 m. The pulling force reaches the maximum of 70 N when y_s = 0.23 m. When the charging process ends at y_s = 0.08 m, the force decreases to 31 N.

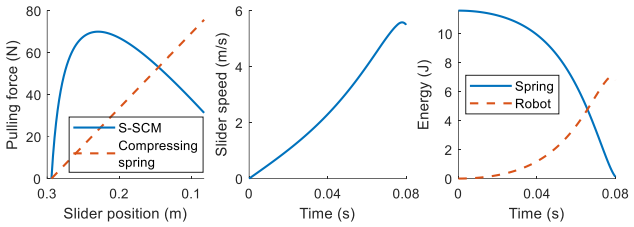

(a) (b) (c)

Fig. 3. Simulation results of the S-SCM. (a) Variation of rope-pulling force in the charging stage. (b) Variation of slider speed in the ejecting stage. (c) Variation of energy in the ejecting stage.

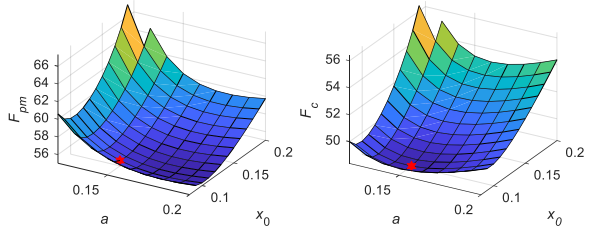

(a) (b)

Fig. 4. Simulation results for optimizing the link length and spring length. (a) The maximum rope-pulling force. (b) The cost function value.

The ejecting process was simulated by solving (5). As a result, Fig. 3(b) shows the variation of the slider's velocity. It is observable that the slider's speed continuously rises to 5.6 m/s at 0.077 s, indicating the takeoff speed. Fig. 3(c) exhibits the variations of the spring and robot's energy values. The spring stores 11.6 J energy at the beginning. When the ejecting process ends at 0.077 s, 62% of the spring's energy is converted to the robot. The lost energy is converted to the mechanical energy of the ejector's components.

We also compared the S-SCM with the case of only using a compressing spring between the root link and the slider. The compressing stiffness needs to be 355 N/m to provide the same takeoff energy as the case of S-SCM. According to Fig. 3(a), the maximum pulling force is 70 N for the S-SCM and 75 N for the compressing spring. This means the S-SCM requires a lower output torque from the winch motor.

C. Structural Optimization

Under the objective of satisfying the desired takeoff speed, the linkage lengths and spring elasticity of the S-SCM are optimized to improve energy efficiency and reduce motor load. The maximum mass of the FWR is configured as 0.45 kg. The flapping frequency is 4 Hz, and the wingspan is 1 m. The wing-flapping motion must provide sufficient lift force when takeoff. According to our previous research [16], when the airspeed is 5 m/s and the pitch angle is 20°, the flapping motion at 2 Hz provides a lift force of 2.3 N. Since the flapping frequency in this work is 4 Hz, the generated lift force is approximately 4.6 N, exceeding the robot's weight. Therefore, the takeoff speed of 5 m/s is sufficient.

The maximum takeoff acceleration is assumed to be 60 m/s^2 to protect the robot from breaking. That means the sliding distance is at least 0.2 m to reach the desired takeoff speed. Upon these design indexes, the side link length a and spring length x_0 are optimized through simulations. The line density of the side link and the tensile spring are configured as 0.3 kg/m and 0.6 kg/m, respectively. The energy efficiency is approximated from the weight values:

$$\tilde{\eta} = m_4 / \sum_{i=1}^{5} m_i \tag{6}$$

The energy required to be stored in the spring is

$$E_s = 0.5 m_4 v_T^{\,2} / \tilde{\eta} \tag{7}$$

where v_T is the target takeoff speed. If the original spring length x_0 is given, the spring length at the end of the charging stage is

$$x_1 = b + 2\sqrt{a^2 - \left(\frac{y_0 - \Delta y_s}{2}\right)^2},\ y_0 = 2\sqrt{a^2 - \left(\frac{x_0 - b}{2}\right)^2} \tag{8}$$

where Δy_s is the sliding distance of the slider, y_0 is the slider's position when the spring length is x_0. The desired spring elasticity is obtained from (7)(8):

$$k = 2E_s / (x_1 - x_0)^2 \tag{9}$$

The optimization problem is formulated as

$$\begin{cases} \min\ F_c(a, x_0) = 100 k_w (1 - \tilde{\eta}) + (1 - k_w) F_{pm} \\ \text{s.t. } m_4 = 0.45\text{kg}, \Delta y_s = 0.2\text{m}, v_T = 0.5\text{m/s} \end{cases} \tag{10}$$

where $F_c(a, x_0)$ is the cost function that penalizes the loss of energy and the maximum pulling force of the rope, the weight factor k_w is configured as 0.35.

Problem (10) is solved by static simulations based on (3) and (6) to (9). The results are shown in Fig. 4. As shown in Fig. 4(a), a larger link length and a smaller spring length help to reduce the pulling force. F_{pm} reaches the minimum of 55 N when a = 0.18 m and x_0 = 0.11 m. However, long links affect energy efficiency, hence increasing the cost. It is shown in Fig. 4(b) that the cost function reaches the minimum of 48.3 when a = 0.15 m and x_0 = 0.1 m. The corresponding spring elasticity is 277 N/m, and the maximum pulling force is 56 N.

III. System Design and Fabrication

This section introduces the mechanism design and working procedure of the FWR-ejecting system.

A. Ejecting Mechanism and FWR

Fig. 5(a) shows the CAD model of the ejector. It is composed of the pitch mechanism, winch mechanism, and S-SCM. The pitch mechanism is the basis of the ejector. It holds the upper modules through a pitch shaft. The pitch motor adjusts the pitch angle of the ejector. The winch mechanism is a gear system that realizes the retracting and releasing of the rope. As shown in Fig. 5(c), the winch motor's output torque is transmitted to the winch via the intermediate gear. However, the winch gear only engages with half of the intermediate gear, where several teeth are cut off. This gap interrupts the power transmission to the winch.

The S-SCM realizes the structure in Fig. 2. As shown in Fig. 5(b), the slider has a T-shaped slot structure at its front surface. The slot engages with the mini-slider at the bottom of the FWR, which only weighs 3.2 grams. The structure allows automatic disengagement when the FWR moves quicker than

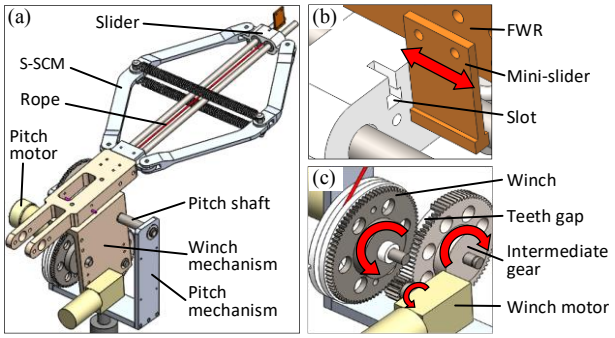

Fig. 5. CAD model of the ejecting mechanism. (a) General view. (b) Detailed view of the slider. (c) Detailed view of the winch mechanism.

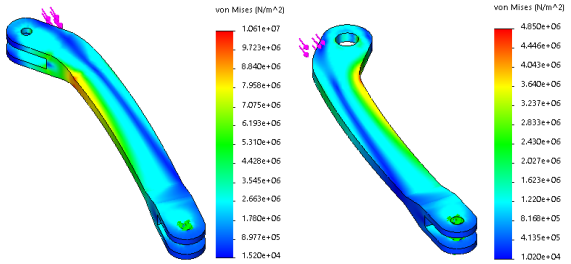

(a) (b)

Fig. 6. Stress analysis result of the side links under the pushing force of 94 N. (a) The bottomed link. (b) The topped link.

the slider. As shown in Fig. 7, the flapping robot has a mass of 270 g and a wingspan of 1 m. A brushless motor provides the power for flapping motion. The tail wing can perform pitching and rolling motions. The flight control board has a JY-62 module that measures the 3-axis attitude angles and accelerations of the robot. A remote-control joystick realizes manipulation of the FWR.

B. *Ejecting Procedure*

The ejecting mechanism is designed to convert between different working stages with little control effort. The working cycle procedure is explained here. Initially, the FWR is attached to the slider through the slot structure. In the charging stage, the winch motor drives the winch to retract the rope. The FWR moves backward with the slider. The motor's output power is transmitted to the spring's potential energy. The red arrows in Fig. 5(c) show the gears' rotating directions in this stage.

When the teeth gap of the intermediate gear reaches the winch gear, the winch is disengaged. At this moment, the spring retracts and releases its potential energy. The slider pushes the FWR to move forward. When the spring recovers its original length, the slider slows down. The FWR detaches from the slider due to the inertial to move forward. In the takeoff stage, once the FWR detects an abrupt change of acceleration, it begins flapping its wings. Proper control of the tail wing will contribute to a successful takeoff.

C. *Prototype Manufacture*

The winch motor was selected according to the payload. Fig. 3(a) shows that the rope's pulling force is 70 N at most. Hence, the 69-mm winch requires a torque of 2.4 Nm. The winch motor was selected as a JGY-395 motor with a 252 times reduction. The rated speed and torque of the motor are 23 rpm and 1.8 Nm, respectively. The motor rotates 5.23 cycles in a single charging stage, suggesting a working time of 16.5 s.

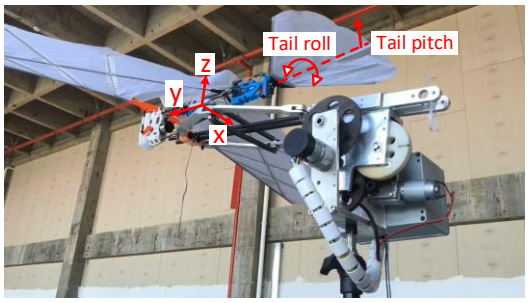

Fig. 7. The prototypes of the ejector and the FWR.

A stress analysis was conducted to confirm the strength of the aluminum side links. Since each side link is a two-force element, the maximum payload of the side link is $F_{sm} = 2aF_{pm}/y_m$, where y_m is the slider's position when the pulling force is the largest ($F_p = F_{pm}$). Substituting the link length values and the spring stiffness given in Section II.B, the maximum payload of each side link is 94 N. As shown in Fig. 6, the maximum stress of the topped link is 10.6 MPa, which is 38% of the yield stress. The stress of the bottomed link is 4.85 MPa. Therefore, the side links can endure the payload. Fig. 7 shows the prototypes of the ejector and the FWR. The robot's body frame and the tail's motions are marked in the figure.

IV. Experiments and Discussions

This section presents the results of three sections of experiments concerning the charging, ejecting, and takeoff stages, respectively.

A. *Charging Experiment*

The energy-charging stage was investigated first. The structural parameters of the ejector were the same as those of the simulations in Section II.B. During the charging phase, the controlling board of the ejector measured the power of the winch motor and the angle of the winch. The results are plotted in Fig. 8.

It is shown in Fig. 8(a) that there is a startup power of 15.7 W at the beginning time of 1.6 s. After that, the power increases from 2 W to 11 W until 5.8 s, then slowly decreases to 5.4 W when the charging process is finished. Therefore, the trend of motor power generally complies with the pulling force shown in Fig. 3(a). According to Fig. 8(b), the winch speed remains relatively steady, varying slightly between 17 to 22 °/s. The final peak value at 19.6 s is due to the quick motion when the winch is released. It is also noticeable from Fig. 8 that the charging process takes 18.5 seconds. The results indicate that the charging process is quick and steady, laying a foundation for the ejecting and takeoff stages.

B. *Static Ejecting Experiment*

Static ejecting experiments were conducted to evaluate the ejector's performance. The experiment setup can be seen in

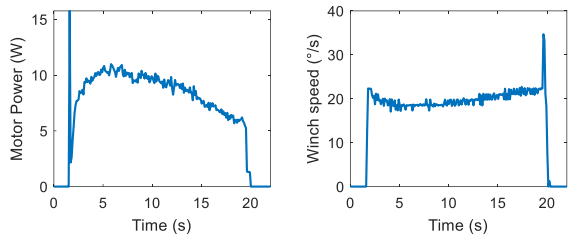

(a) (b)

Fig. 8. Experiment results of the charging stage. (a) Winch motor power. (b) Winch speed.

Fig. 9(a). The robot did not flap its wings, so it fell onto the safety net. The ejector was 1.9 m above the ground. The pitch angle of the ejector was 9°. Two tests are conducted. In test 1, the tail wing kept the original pitch angle. In test 2, the pitch angle of the tail was lowered by 5° during the ejecting stage. The experiment results are shown in Fig. 9. Fig. 9(a) is a stroboscopic motion image with frame intervals of 0.1 seconds. Fig. 9(b)(c) show the variations of the robot's pitch angle and speed, respectively.

The result of test 1 is analyzed. The robot begins to accelerate from 0 s with the original pitch angle of 8.3° (Fig. 9(b)). The robot detaches the ejector at 0.1 s. At this moment, the vertical speed is the maximum (1.1 m/s in Fig. 9(c)), and the pitch angle has a peak of 27° (Fig. 9(b)). At 0.2 s, the horizontal speed peaks at 3.8 m/s, and the pitch angle drops to 19°. From 0.2 s to the end, the horizontal speed steadily decreases to 3.74 °/s. Around 0.64 s, the pitch angle experiences another peak of 40.4°, and the vertical speed begins to dive, indicating that the robot stalls and descends. It finally lands 2.3 m away from the ejector.

The results of test 1 show that the robot experiences an undesired increase in pitch angle. This results from the slider's pushing force being below the robot's mass centroid, and the robot endures a flip torque. To alleviate this, we lowered the tail wing by 5° in test 2. It is apparent in Fig. 9 that the maximum pitch angle in test 2 is decreased by 1.1°, the speed reduction is slowed, and the gliding distance of the robot is extended by 0.3 m.

From the maximum speed values in horizontal and vertical directions, the total takeoff speed is 4 m/s. 11.6-J energy is stored in the spring, and 18% is converted to the robot's kinetic energy. The takeoff speed and energy efficiency are smaller than the simulation results (5.6 m/s and 62%). The loss of energy is assumed to result from several reasons. First, the air resistance and friction force are not modeled. Second, the point of force from the ejector is below the FWR's centroid, causing the robot to undergo self-flip and collision with the ejector. Finally, the reaction force from the FWR drives the ejector to vibrate, absorbing part of the spring's energy.

C. *Takeoff Experiment*

In the takeoff experiment, the robot began to flap its wings at 4.5 Hz once detecting a surge of forward acceleration. The pitch of the tail was manually controlled, and the tail's roll

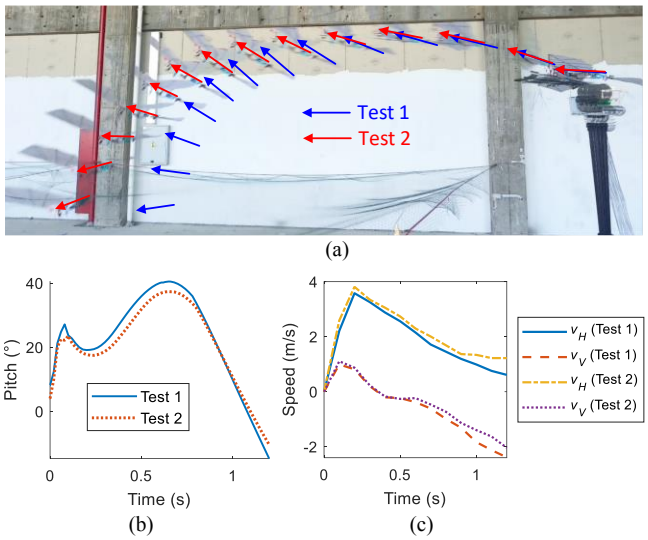

(a) (b) (c)

Fig. 9. Experiment results of the static ejecting section. (a) Photographic record of the robot's trajectory. (b) Pitch angle of the robot. (c) Velocity of the robot. v_H: horizontal velocity, v_V: vertical velocity.

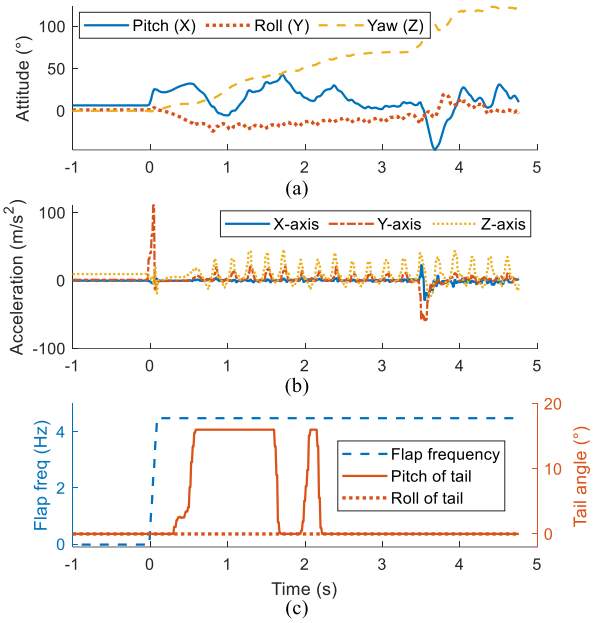

(a) (b) (c)

Fig. 10. Experiment results of the takeoff section. (a) Three-axes attitude of the robot. (b) Three-axes acceleration of the robot. (c) Control pulse widths of the robot's motors.

angle was kept unchanged. Fig. 10 shows variations in the robot's attitudes, accelerations, and motor control signals. Fig. 11 is the stroboscopic motion image with 0.2-s intervals.

As shown in Fig. 10(b), the robot is launched at 0 s. The spike of Y-axis acceleration stimulates the flapping control signal, while the execution of the flapping motor has a time delay. At 0.5 s, the pitch angle peaks at 32° due to the tilt torque observed in the static ejecting experiment. Meanwhile, the Z-axis acceleration begins to oscillate as a reflection of the wing-flapping motion. At 1 s, the pitch angle decreases to −5°, complying with the static results in Fig. 9(b). At the same time, the tail is raised to prevent the robot from crashing. At 1.5 s, the altitude of the robot reaches the minimal point. The pitch

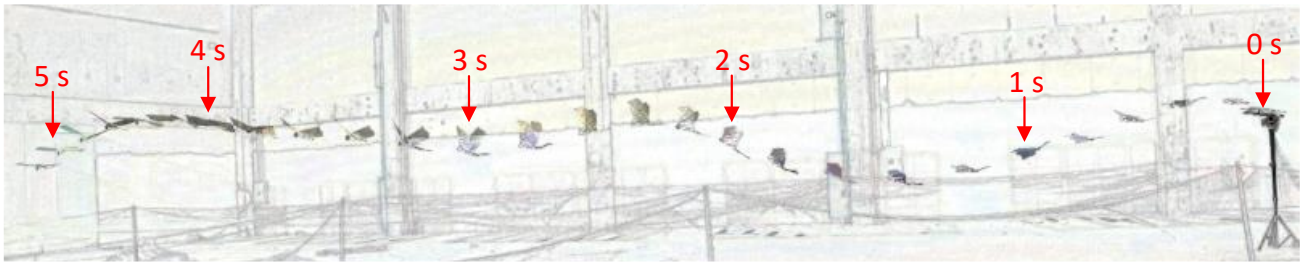

Fig. 11. Photographic record of the robot's trajectory in the takeoff experiment.

angle increases, and the flapping motion provides lift and thrust forces. From 2 s, the robot enters the cruise state. Therefore, although the initial speed is slower than the simulation, the FWR can still successfully take off from a sufficient height.

Besides, it is noticeable in Fig. 10(a) that the roll angle is mostly negative during the flight, which drives the yaw angle to stray. This deviation can be attributed to the slight asymmetry in the robot's aerodynamic properties and the absence of a closed-loop control system for the yaw angle.

Finally, we evaluated the performance of the ejector in terms of success rate and cycle time. The ejecting takeoff method was conducted 10 times, and 9 trials successfully launched the robot. The only failure was attributed to the improper control of the tail. The charging process takes 18 seconds. Installing the robot onto the ejector takes another 10 seconds, so the ejector's working cycle is 28 seconds. Therefore, the ejector has a high success rate and a short working cycle time. It helps to save on training costs and workforce when launching FWRs.

V. Conclusion and Future Work

This work presents an FWR ejector to realize autonomous takeoff of the robots. The system requires little additional payload to the FWR and can be deployed in almost all terrain conditions. Models for the charging and ejecting stages are established and then used for the optimization design of the structure. The ejector improves the success rate and operation speed compared to manual throwing. The experiment results indicate that the ejector generates a takeoff speed of 4 m/s. The robot manages to enter the cruise state after takeoff. The research results are valuable for pushing forward the application of FWRs. Nonetheless, drawbacks are exposed. The dynamic model does not consider the effects of air resistance and friction. Additionally, the current slot structure engaging the FWR introduces additional energy loss. Furthermore, the motion of the tail wing is still manually controlled. These issues will be solved in the future.

References

[1] M. Karásek, F. T. Muijres, C. De Wagter, B. D. W. Remes, and G. C. H. E. de Croon, "A tailless aerial robotic flapper reveals that flies use torque coupling in rapid banked turns," *Science*, vol. 361, no. 6407, pp. 1089–1094, Sep. 2018.

[2] T. Ozaki, N. Ohta, T. Jimbo, and K. Hamaguchi, "Takeoff of a 2.1 g Fully Untethered Tailless Flapping-Wing Micro Aerial Vehicle with Integrated Battery," *IEEE Robot. Autom. Lett.*, vol. 8, no. 6, pp. 3574–3580, Jun. 2023.

[3] H. Huang, W. He, J. Wang, L. Zhang, and Q. Fu, "An All Servo-Driven Bird-Like Flapping-Wing Aerial Robot Capable of Autonomous Flight," *IEEE/ASME Trans. Mechatron.*, vol. 27, no. 6, pp. 5484–5494, Dec. 2022.

[4] R. Zufferey *et al.*, "Design of the High-Payload Flapping Wing Robot E-Flap," *IEEE Robot. Autom. Lett.*, vol. 6, no. 2, pp. 3097–3104, Apr. 2021.

[5] J. Hoff, N. Jeon, P. Li, and J. Kim, "Bat Bot 2.0: bio-inspired anisotropic skin, passive wrist joints, and redesigned flapping mechanism," in *IEEE Int. Conf. Intell. Rob. Syst., IROS*, Prague, Czech Republic: IEEE, Sep. 2021, pp. 8424–8430.

[6] X. Fan, K. Breuer, and H. Vejdani, "Wing Fold and Twist Greatly Improves Flight Efficiency for Bat-Scale Flapping Wing Robots," in *IEEE Int. Conf. Intell. Rob. Syst., IROS*, Prague, Czech Republic: IEEE, Sep. 2021, pp. 7391–7397.

[7] E. Sihite, P. Ghanem, A. Salagame, and A. Ramezani, "Unsteady aerodynamic modeling of Aerobat using lifting line theory and Wagner's function," in *IEEE Int. Conf. Intell. Rob. Syst., IROS*, Kyoto, Japan: IEEE, Oct. 2022, pp. 10493–10500.

[8] R. Tapia *et al.*, "A Comparison Between Framed-Based and Event-Based Cameras for Flapping-Wing Robot Perception," in *IEEE Int. Conf. Intell. Rob. Syst., IROS*, Detroit, MI, USA: IEEE, Oct. 2023, pp. 3025–3032.

[9] S. Zhong, S. Wang, W. Xu, J. Liu, and E. Pan, "Autonomous flight control with different strategies applied during the complete flight cycle for flapping-wing flying robots," *Sci. China-Technol. Sci.*, Sep. 2023.

[10] D. Ma, B. Song, Z. Wang, J. Xuan, and D. Xue, "Development of a Bird-like Flapping-wing Aerial Vehicle with Autonomous Take-off and Landing Capabilities," *J. Bionic Eng.*, vol. 18, no. 6, pp. 1291–1303, Nov. 2021.

[11] M. L. Afakh, T. Sato, H. Sato, and N. Takesue, "Development of Flapping Robot with Self-Takeoff from The Ground Capability," in *IEEE Int. Conf. Rob. Autom., ICRA*, May 2021, pp. 321–327.

[12] N. Zhao *et al.*, "A Self-Balanced Vehicle Base for Takeoff of a Flapping-Wing Robot," in *IEEE Int. Conf. Adv. Robot Mechatronics, ICARM*, 2022, pp. 593–598.

[13] J. Zhang, C. Dong, A. Song, and IEEE, "Jumping Aided Takeoff: Conceptual Design of a Bio-Inspired Jumping-Flapping Multi-Modal Locomotion Robot," in *IEEE Int. Conf. Robot Biomimetics, ROBIO*, 2017, pp. 32–37.

[14] Y. Zhao, F. Liu, Y. Hao, and W. Shao, "Design and analysis of folding wing Bionic Ornithopter," in *SPIE Int. Soc. Opt. Eng., ICMLCA*, Dec. 2021, pp. 1–6.

[15] G. Song, K. Yin, Y. Zhou, and X. Cheng, "A Surveillance Robot with Hopping Capabilities for Home Security," *IEEE Trans. Consum. Electron.*, vol. 55, no. 4, pp. 2034–2039, Nov. 2009.

[16] S. Yang, Y. Shen, B. Li, Y. Li, and J. Zhang, "Modeling and Simulation of a Flapping-Wing Robot with Active Tails for Balancing Control during Wheeled Running," in *IEEE Int. Conf. Mechatronics Autom., ICMA*, Changchun: IEEE, Aug. 2018, pp. 1806–1811.